

Data-Free PINNs for Compressible Flows: Mitigating Spectral Bias and Gradient Pathologies via Mach-Guided Scaling and Hybrid Convolutions

Ryosuke Yano^{1*}

¹Tokio Marine dR Co., Ltd., 1-5-1, Otemachi, Chiyoda-ku, Tokyo, 100-0004, Japan.

Corresponding author(s). E-mail(s): ryosuke.yano@tokio-dr.co.jp;

This paper presents a fully data-free Physics-Informed Neural Network (PINN) capable of solving compressible inviscid flows (ranging from supersonic to hypersonic, up to $Ma=15$, where Ma is the Mach number) around a circular cylinder. To overcome the spatial blindness of standard Multi-Layer Perceptrons, a structured hybrid architecture combining radial 1D convolutions with anisotropic azimuthal 2D convolutions is proposed to embed directional inductive biases. For stable optimization across disparate flow regimes, a regime-dependent, Mach-number-guided dynamic residual scaling strategy is introduced. Crucially, this approach scales down residuals to mitigate extreme gradient stiffness in high-Mach regimes, while applying penalty multipliers to overcome the inherent spectral bias and explicitly enforce weak shock discontinuities in low-supersonic flows. Furthermore, to establish a global thermodynamic anchor essential for stable shock wave capturing, exact analytical solutions at the stagnation point are embedded into the loss formulation. This is coupled with a novel "Upstream Fixing" boundary loss and a Total Variation (TV) loss to explicitly suppress upstream noise and the non-physical carbuncle phenomenon. The proposed framework successfully captures the detached bow shock without referential data. While the requisite artificial viscosity yields a slightly thicker shock wave compared to computational fluid dynamics, the proposed method demonstrates unprecedented stability and physical fidelity for data-free PINNs in extreme aerodynamics.

Introduction

Physics-Informed Neural Networks (PINNs) have revolutionized Scientific Machine Learning (SciML) by enabling mesh-free solutions to partial differential equations (PDEs) [1]. While PINNs offer significant advantages over traditional Computational Fluid Dynamics (CFD) in inverse problems, their application to high-speed compressible aerodynamics remains severely limited, particularly when referential training data is unavailable. Although the Universal Approximation Theorem [2] suggests that neural networks can theoretically represent complex flow fields, solving hyperbolic conservation laws in a purely data-free regime presents a formidable optimization challenge. Unlike parabolic or elliptic systems, where physical diffusion naturally smooths the solution space [3], the inviscid Euler equations admit discontinuous shock solutions. In this context, standard Multi-Layer Perceptrons (MLPs) suffer from *spectral bias* [4]; they struggle to capture high-frequency shock fronts, resulting either in non-physical smearing or convergence to trivial minima due to the absence of data-driven guidance.

To mitigate these instabilities, various compensatory techniques have been proposed. Table 1 summarizes the progressive efforts in applying PINNs to the compressible Euler equations. Early works primarily focused on unsteady 1D Riemann problems (e.g., Sod shock tubes), where initial conditions (IC) and boundary conditions (BC) sufficiently constrain the optimization. For instance, Chaumet and Giesselmann [5] applied foundational PINN formulations to these 1D cases. This was further extended by Mizuno et al. [6], who explicitly incorporated the Equation of State (EOS) to stabilize the resolution of Riemann problems and simple oblique shocks, while Ferrer-Sánchez et al. [7] demonstrated that PINNs could generalize even to General Relativistic Hydrodynamics (GRHD) for Riemann problems.

Moving to 2D domains, Mao et al. [8] successfully simulated stationary oblique shocks by strictly enforcing ICs and BCs. To improve the resolution of sharp discontinuities, Liu et al. [9] directly embedded the Rankine-Hugoniot (RH) jump conditions and explicit conservation laws (CON) into the loss function. Another robust approach to handling discontinuous gradients is the introduction of Artificial Viscosity (AV). Wassing et al. [10] [11] incorporated an adaptive AV model and viscosity-based loss terms (VIS) to smooth oblique shocks without destabilizing the optimizer. However, capturing a detached bow shock around a blunt body remains significantly more challenging due to the complex coupling of a strong normal shock ahead of the stagnation point and highly curved oblique shocks downstream. While Cai et al. [12] and Jagtap et al. [13] successfully simulated such detached bow shocks and expansion waves, their methodologies fundamentally relied on external reference data (e.g., pre-computed CFD results) to guide the neural network.

Consequently, solving the steady-state 2D bow shock problem in a purely *data-free* regime remains an open challenge. It is argued that the fundamental bottleneck lies in the architectural limitations of standard MLPs, which process spatial coordinates as flat feature vectors, thereby lacking any directional or topological context—a phenomenon termed *spatial blindness* [14]. To address this, a *hybrid radial-azimuthal convolutional architecture* is introduced that embeds a physical inductive bias directly into the neural topology. By utilizing large-kernel 1D convolutions ($k = 15$) in the

radial direction, this architecture efficiently propagates upstream boundary information deep into the domain to precisely localize the shock interface.

To overcome the inherent trade-off between optimization stability and shock sharpness without relying on referential data, the proposed framework introduces several crucial innovations (highlighted in Table 1). First, a sophisticated AV strategy is employed that is globally annealed over training epochs and spatially modulated by the local pressure gradient, ensuring that numerical dissipation is strictly localized to the shock layer. Furthermore, to explicitly suppress the non-physical carbuncle phenomenon [15]—a notorious numerical instability near the stagnation region—a Total Variation (TV) penalty is integrated into the loss formulation. Second, a novel “Upstream Fixing” loss term (Mask) is proposed to rigidly stabilize the freestream region and prevent numerical oscillations from propagating upstream of the bow shock. Third, to establish a global thermodynamic anchor essential for determining the correct shock amplitude, the exact analytical solutions at the stagnation point are explicitly embedded into the loss formulation.

Finally, and most crucially, a regime-dependent, Mach-number-guided dynamic residual scaling strategy is implemented to resolve the dual optimization pathologies across different flow speeds. In high-Mach regimes ($Ma \geq 3$), normalizing (scaling down) the momentum and energy PDE losses by factors of the freestream Mach number (Ma^2 and Ma^4 , respectively) acts as a strict mathematical prerequisite to mitigate extreme gradient stiffness [16] and prevent divergence. Conversely, in low-supersonic flows ($Ma = 2$), multiplying (scaling up) these residuals acts as a stringent penalty to overcome the network’s spectral bias, forcing it to explicitly resolve weak shock discontinuities rather than collapsing into smooth, non-physical states.

Ultimately, it is demonstrated that this highly structured approach successfully captures sharp shock discontinuities across a wide range of supersonic and hypersonic flows ($2 \leq Ma \leq 15$) around a circular cylinder—a benchmark where conventional data-free PINNs systematically fail.

Methodology

The present framework assumes an ideal gas with a constant specific heat ratio ($\gamma = 1.4$) to isolate the fundamental mathematical challenge of gradient stiffness in purely data-free optimization, it is important to note that real gas effects—such as vibrational excitation and diatomic molecular dissociation—become physically dominant in extreme hypersonic regimes (e.g., $10 \leq Ma$). As rigorously formulated in our previous kinetic studies [17, 18], these non-equilibrium real gas effects strongly influence the macroscopic shock layer structures. Integrating such complex thermodynamic equations of state into the regime-dependent scaled PINN framework remains an important subject for future work.

Table 1 Comparison of PINN studies for compressible Euler equations. Abbreviations: PDE: Partial Differential Equation residuals; BC: Boundary Conditions; IC: Initial Conditions; RH: Rankine-Hugoniot conditions; CON: Conservation laws; VIS: Artificial Viscosity term; EOS: Equation of State; Mask: Upstream fixing; TV: Total Variation; Data: Reference data.

| Literature (Authors) | Governing Equations | Loss Components | Output Variables | Variables | Problem Types |
|----------------------------|---------------------|------------------------------------|-------------------------------|-----------|--|
| Mao et al. [22] | Euler + EOS | PDE, BC, IC | ρ, \mathbf{u}, p | | Oblique shock |
| Cai et al. [23] | Euler + EOS | PDE, BC, Data | ρ, \mathbf{u}, p | | Bow shock |
| Jagtap et al. [24] | Euler + EOS | PDE, BC, Data | ρ, \mathbf{u}, p | | Expansion wave, Detached shock |
| Liu et al. [26] | Euler + EOS | PDE, BC, IC, RH, CON | ρ, \mathbf{u}, p | | Riemann problem |
| Wassing et al. [27] | Euler + AV + EOS | PDE, BC, IC, VIS | $\rho, \mathbf{u}, p, E, \nu$ | | Inviscid flow, Oblique shock |
| Ferrer-Sánchez et al. [28] | GRHD | PDE, BC, IC | ρ, \mathbf{u}, p | | Riemann problem |
| Chaumet & Giesselmann [29] | Euler + EOS | PDE, BC, IC | ρ, \mathbf{u}, p | | Sod shock tube |
| Mizuno et al. [31] | Euler + EOS | PDE, BC, IC, Explicit EOS | ρ, \mathbf{u}, p, T | | Riemann problem, Oblique shock |
| This work | Euler + EOS | PDE, BC, Mask, Enthalpy, TV | ρ, \mathbf{u}, p | | Supersonic bow shock ($2 \leq \mathbf{Ma}_\infty \leq 15$) |

Governing Equations and Boundary Conditions

The steady-state Euler equations for inviscid compressible flow are solved in this study. The system is defined by the conservation of mass, momentum, and energy:

$$\nabla \cdot (\rho \mathbf{u}) = 0, \quad \nabla \cdot (\rho \mathbf{u} \otimes \mathbf{u} + p \mathbf{I}) = 0, \quad \nabla \cdot ((E + p) \mathbf{u}) = 0, \quad (1)$$

where ρ is the density, \mathbf{u} is the velocity vector, p is the pressure, and E is the total energy.

To close the system of equations for the flow over a circular cylinder, the following boundary conditions are imposed:

- **Inflow (Free-stream) Condition:** At the upstream far-field boundary, the flow variables are prescribed to match the free-stream conditions: $\rho = \rho_\infty$, $u = u_\infty$, $v = 0$, and $p = p_\infty$ (subscript ∞ indicates the free-stream state). In this study, these values are normalized such that $\rho_\infty = 1$ and $u_\infty = \text{Ma}_\infty$, where Ma_∞ is the free-stream Mach number and $T_\infty = 1/\gamma$ ($\gamma = 1.4$: specific heat) is the free-stream normalized temperature.
- **Slip Wall Condition:** On the solid surface of the cylinder, the inviscid nature of the Euler equations requires a slip boundary condition: $\mathbf{u} \cdot \mathbf{n} = 0$, where \mathbf{n} is the unit normal vector.
- **Symmetry Condition:** Given the geometric symmetry, a symmetry boundary condition is applied along the stagnation line ($y = 0$): $v = 0$, $\partial\rho/\partial y = 0$, $\partial u/\partial y = 0$, and $\partial p/\partial y = 0$. This ensures flow consistency and allows for a half-domain simulation to reduce computational costs.

Network Design Philosophy: Directional Inductive Bias

Before detailing the specific layer configurations, the underlying design philosophy of the proposed architecture is established. Standard Multi-Layer Perceptrons (MLPs) treat spatial coordinates merely as flat, independent input features. This isotropic treatment of space inherently ignores the anisotropic nature of high-speed fluid dynamics. The steady Euler equation governing supersonic flow over the blunt body exhibits distinct directional characteristics: the radial direction is dominated by hyperbolic wave propagation and sharp discontinuities (shock waves), while the azimuthal direction is characterized by elliptic-like smooth isentropic expansion and geometric symmetry.

To resolve this without relying on external reference data, the proposed architecture incorporates a *directional inductive bias* explicitly tailored to the physics of the polar Euler equations. The spatial processing is deliberately decoupled into two orthogonal operations:

- 1) A large-kernel 1D convolution along the radial axis to capture long-range upstream-downstream inter-dependencies, allowing the network to anchor the detached bow shock between the free-stream and the wall.
- 2) An anisotropic 2D convolution along the azimuthal axis, preserving the continuous (r, θ) grid topology to mathematically mimic the tangential finite-difference operators (e.g., $\frac{1}{r} \frac{\partial}{\partial \theta}$) inherent to the governing PDEs.

Mathematical Formulation of the Hybrid Convolutional Architecture

The inability of standard Multi-Layer Perceptrons (MLPs) to sharply resolve shock waves can be rigorously explained through the lens of the *Spectral Bias* phenomenon

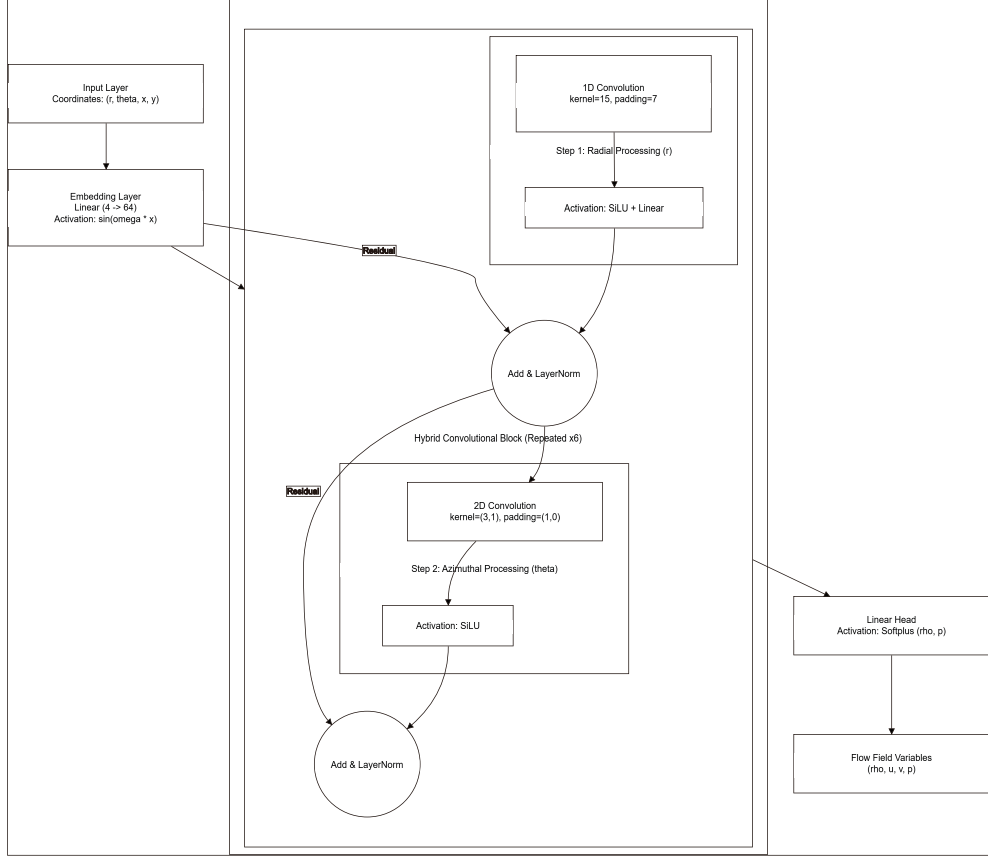


Fig. 1 Schematic of the proposed Hybrid Convolutional PINN architecture. The network processes input spatial coordinates via a Fourier feature embedding layer, followed by a stack of $L = 6$ Hybrid Convolutional Blocks. Each block sequentially applies a large-kernel radial 1D convolution and an anisotropic azimuthal 2D convolution to embed directional physical inductive biases. Finally, the processed hidden states are mapped to the macroscopic flow variables (ρ, u, v, p) through a Multi-Layer Perceptron (MLP) decoder equipped with Softplus-based positivity constraints to ensure thermodynamic realizability.

[4] and Neural Tangent Kernel (NTK) theory [19].

A shock wave mathematically represents a jump discontinuity in the flow-field. Approximating such a step-like function $f(x)$ requires an infinite sum of high-frequency components. For instance, the Fourier series expansion of a simplified shock discontinuity centered at the origin can be expressed as:

$$f(x) \propto \sum_{k=1,3,5,\dots}^{\infty} \frac{1}{k} \sin(kx), \quad (2)$$

where k denotes the frequency. Equation (2) highlights that high-frequency modes ($k \gg 1$) are absolutely indispensable for resolving the sharp interface, and their

required amplitudes decay relatively slowly at a rate of $\mathcal{O}(k^{-1})$.

Conversely, the learning dynamics of a sufficiently wide MLP trained by continuous-time gradient descent can be described by the NTK. Let $E_k(t)$ be the network’s prediction error of the frequency component k at training time t , and η be the learning rate.

The evolution of the error follows the linear ordinary differential equation:

$$\frac{dE_k(t)}{dt} = -\eta\lambda_k E_k(t), \quad (3)$$

where λ_k is the eigenvalue of the NTK corresponding to the frequency k . Solving this yields an exponential decay of the error over time:

$$E_k(t) = E_k(0) \exp(-\eta\lambda_k t). \quad (4)$$

According to the spectral bias theory [4], for a standard MLP with a ReLU activation function in a d -dimensional input space, the eigenvalues decay polynomially with respect to the frequency:

$$\lambda_k = \mathcal{O}(k^{-(d+1)}). \quad (5)$$

In a 1D spatial domain ($d = 1$), the learning speed for a specific frequency drops dramatically as $\lambda_k \propto k^{-2}$.

When reconciling the physical requirements of a shock wave with the learning capacity of an MLP, a critical theoretical bottleneck emerges. By substituting Eq. (5) into Eq. (4), the error decay for a high-frequency component k becomes:

$$E_k(t) = E_k(0) \exp\left(-\eta\frac{\hat{C}}{k^2}t\right), \quad (6)$$

where \hat{C} is a positive constant. As k becomes large — which is strictly required for shock resolution — the exponent term approaches zero ($\eta\hat{C}t/k^2 \rightarrow 0$). Consequently, $\exp(-\eta\hat{C}t/k^2) \approx 1$, leading to:

$$E_k(t) \approx E_k(0). \quad (7)$$

This mathematical formulation proves that while low-frequency components ($k \rightarrow 0$) converge almost instantaneously, the error for high-frequency components ($k \rightarrow \infty$) remains virtually unchanged over any practically achievable training duration t . As a result, the standard MLP acts inherently as a low-pass filter, inevitably yielding a smeared, diffuse gradient rather than a physically accurate sharp shock discontinuity. The proposed Physics-Informed Neural Network is structured upon a body-fitted discrete grid ($N_r \times N_\theta$). The architecture consists of an embedding layer, a stack of $L = 6$ identical Hybrid Convolutional Blocks, and a decoding Multi-Layer Perceptron (MLP) head as shown in Fig. 1.

1. Spatial Embedding Layer

To overcome the spectral bias of neural networks and enable the resolution of high-frequency shock gradients, the 4-dimensional physical coordinate vector $\boldsymbol{\xi}_{i,j} = [r_{i,j}, \theta_{i,j}, x_{i,j}, y_{i,j}]^T$ at each grid node (i, j) is projected into a high-dimensional feature space using a Fourier feature embedding. Let $\mathbf{Z}^{(0)} \in \mathbb{R}^{C \times N_r \times N_\theta}$ denote the initial feature tensor with channel dimension $C = 64$. The embedding operation is defined as:

$$\mathbf{Z}_{:,i,j}^{(0)} = \sin(S_{freq} \cdot (\mathbf{W}_{emb} \boldsymbol{\xi}_{i,j} + \mathbf{b}_{emb})) \quad (8)$$

where $\mathbf{W}_{emb} \in \mathbb{R}^{C \times 4}$ and $\mathbf{b}_{emb} \in \mathbb{R}^C$ are trainable weights and biases, and S_{freq} is a predefined frequency scaling factor.

2. Radial 1D Convolutional Formulation

Within the l -th Hybrid Convolutional Block ($l = 1, \dots, 6$), the feature tensor $\mathbf{Z}^{(l-1)}$ is first processed along the radial streamlines. To capture the profound thermodynamic jump across the shock wave, the feature map is treated as N_θ independent 1D sequences of length N_r . A 1D convolution with a large receptive field (kernel size $K_r = 15$) is applied exclusively along the radial index i . Mathematically, the radial feature extraction for the c -th channel is formulated as:

$$\tilde{\mathbf{F}}_{rad,c,i,j} = \sum_{c'=1}^C \sum_{k=-\lfloor K_r/2 \rfloor}^{\lfloor K_r/2 \rfloor} \mathbf{W}_{rad,c,c'}^{(k)} \mathbf{Z}_{c',i+k,j}^{(l-1)} + \mathbf{b}_{rad,c} \quad (9)$$

where zero-padding is applied to the radial boundaries to maintain spatial dimensions. This effectively bridges the physical gap between the unperturbed freestream and the stagnation region without cross-contaminating azimuthal angles. The intermediate state $\mathbf{H}^{(l)}$ is subsequently formed via a linear projection, a SiLU activation (σ), a residual connection, and Layer Normalization (LN):

$$\mathbf{H}_{:,i,j}^{(l)} = \text{LN} \left(\mathbf{Z}_{:,i,j}^{(l-1)} + \mathbf{W}_{proj} \sigma(\tilde{\mathbf{F}}_{rad, :, i, j}) + \mathbf{b}_{proj} \right) \quad (10)$$

3. Azimuthal Anisotropic 2D Convolutional Formulation

Following the radial processing, the intermediate tensor $\mathbf{H}^{(l)}$ is subjected to azimuthal feature mixing. Employing a standard 1D convolution here would necessitate flattening the spatial dimensions, irreparably destroying the 2-dimensional geometric topology. To preserve the exact physical proximity of the structured mesh, a 2D convolution with a highly anisotropic kernel size of $K_r \times K_\theta = 1 \times 3$ is deployed. This directional filter strictly isolates the radial dimension while computing localized spatial correlations across adjacent azimuthal angles:

$$\mathbf{F}_{azi,c,i,j} = \sum_{c'=1}^C \sum_{m=-1}^1 \mathbf{W}_{azi,c,c'}^{(0,m)} \mathbf{H}_{c',i,j+m}^{(l)} + \mathbf{b}_{azi,c} \quad (11)$$

Notice that the radial spatial index offset is rigidly fixed to zero. This localized operation mathematically simulates a trainable finite-difference stencil (analogous to $\frac{\partial \mathbf{U}}{\partial \theta}$), embedding physical continuity directly into the forward pass. The final output of the l -th block is obtained via a second residual skip connection and Layer Normalization:

$$\mathbf{Z}_{:,i,j}^{(l)} = \text{LN} \left(\mathbf{H}_{:,i,j}^{(l)} + \sigma(\mathbf{F}_{azi, :, i,j}) \right) \quad (12)$$

4. State Decoding and Positivity Constraints

After passing through all $L = 6$ blocks, the deeply processed spatial features $\mathbf{Z}_{i,j}^{(L)}$ are mapped back to the macroscopic physical state variables via a point-wise MLP decoder.

$$[\hat{U}_\rho, \hat{U}_u, \hat{U}_v, \hat{U}_p]_{i,j}^T = \text{MLP} \left(\mathbf{Z}_{:,i,j}^{(L)} \right) \quad (13)$$

To strictly adhere to the fundamental thermodynamic laws, density ρ and pressure p must be strictly positive definite everywhere in the flow field. This physical constraint is enforced a priori using a Softplus activation function with small baseline offsets ($\epsilon_\rho, \epsilon_p$):

$$\rho_{i,j} = \ln(1 + \exp(\hat{U}_{\rho,i,j})) + \epsilon_\rho \quad (14)$$

$$p_{i,j} = \ln(1 + \exp(\hat{U}_{p,i,j})) + \epsilon_p \quad (15)$$

$$u_{i,j} = \hat{U}_{u,i,j}, \quad v_{i,j} = \hat{U}_{v,i,j} \quad (16)$$

This ensures the physical realizability of the predicted state vectors before they are subjected to the modified Euler residuals and equation of state.

Physics-Informed Constraints and Artificial Viscosity

To capture sharp shock discontinuities and stabilize numerical oscillations at high Mach numbers, a scalar artificial viscosity ν calculated via a 5-point discrete Laplacian filter ($\Delta \mathbf{U}_{i,j}$) is introduced. The modified Euler residuals for mass and momentum conservation are formulated as:

$$\mathcal{R}_{mass} = \nabla \cdot (\rho \mathbf{u}) - \nu \Delta \rho \quad (17)$$

$$\mathcal{R}_{mom} = \nabla \cdot (\rho \mathbf{u} \otimes \mathbf{u} + p \mathbf{I}) - \nu \Delta (\rho \mathbf{u}) \quad (18)$$

While adding $\nu \Delta \rho$ violates strict macroscopic mass conservation, rigorous introduction of a spatially varying viscosity $\nu(\mathbf{x})$ into the viscous flux $\mathbf{F}_{visc} = \nu(\mathbf{x}) \nabla \mathbf{U}$ forces AD to apply the product rule: $\nabla \cdot (\nu(\mathbf{x}) \nabla \mathbf{U}) = \nu(\mathbf{x}) \Delta \mathbf{U} + \nabla \nu(\mathbf{x}) \cdot \nabla \mathbf{U}$. At the shock, the spike in $\nabla \nu(\mathbf{x})$ acts as an infinitely large non-conservative source term, destroying the Rankine-Hugoniot conditions. Thus, directly appending only the dissipative Laplacian serves as a necessary and robust mathematical compromise to stabilize optimization without residual explosion.

Loss Function Formulation

As schematically summarized in Fig. 2, our training objective combines globally evaluated physical constraints (Mach-scaled Euler residuals L_{pde} and the enthalpy constraint L_H) with region-specific penalty terms that stabilize fully data-free optimization—namely the upstream fixing mask L_{mask} , the localized nose-region penalty L_{nose} , and the stagnation-point anchor L_{stag} —in addition to standard boundary losses (L_{in} , L_{wall} , L_{sym}) and an azimuthal TV regularizer L_{tv} . The training

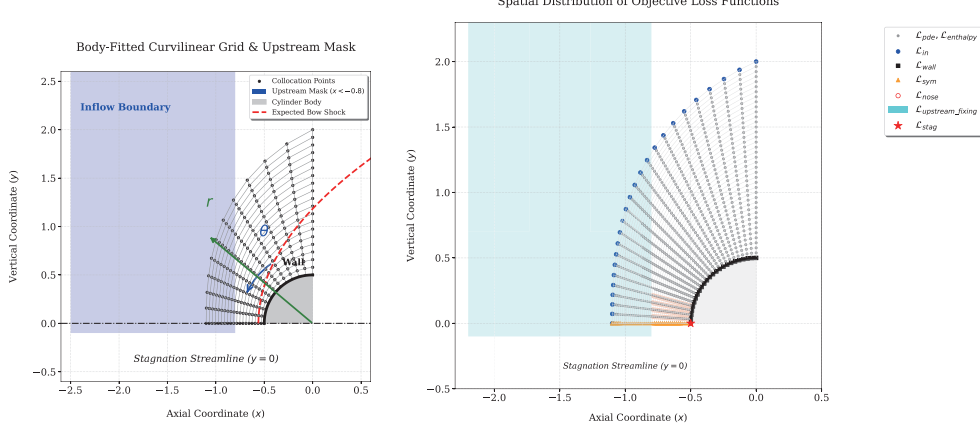


Fig. 2 Schematic representation of the computational domain (left frame) and the spatial distribution of the composite loss function components (right frame). The physical boundary conditions are strictly enforced via localized penalty terms: freestream inflow (\mathcal{L}_{in}), solid slip wall (\mathcal{L}_{wall}), and geometric symmetry (\mathcal{L}_{sym}). To stabilize the purely data-free optimization, specific regional constraints are introduced: an upstream fixing mask (\mathcal{L}_{mask}) to prevent non-physical pre-shock oscillations, a localized nose region penalty (\mathcal{L}_{nose}) to enforce sharp shock resolution, and a pointwise stagnation anchor (\mathcal{L}_{stag}) to calibrate the macroscopic thermodynamic amplitude. Additionally, a Total Variation penalty (\mathcal{L}_{tv}) is applied azimuthally to suppress carbuncle instabilities, while the Mach-scaled Euler PDE residuals (\mathcal{L}_{pde}) and enthalpy conservation (\mathcal{L}_H) are evaluated globally across the continuous fluid domain.

objective minimizes a composite loss function \mathcal{L}_{total} :

$$\mathcal{L}_{total} = \mathcal{L}_{pde} + \lambda_H \mathcal{L}_H + \lambda_{nose} \mathcal{L}_{nose} + \lambda_{in} \mathcal{L}_{in} + \lambda_{wall} \mathcal{L}_{wall} + \lambda_{stag} \mathcal{L}_{stag} + \lambda_{sym} \mathcal{L}_{sym} + \lambda_{mask} \mathcal{L}_{mask} + \lambda_{tv} \mathcal{L}_{tv} \quad (19)$$

- **Euler Residual Loss (\mathcal{L}_{pde}):** To achieve a balanced optimization landscape across disparate physical scales, a *Mach-number-based dynamic residual scaling* is introduced. Momentum and energy residuals are weighted with Ma_∞^{-2} and Ma_∞^{-4} respectively for $3 \leq \text{Ma}_\infty$ (i.e., PINN type A) or Ma_∞^2 and Ma_∞^4 respectively for $\text{Ma}_\infty \leq 2$ (PINN type B) as

$$\mathcal{L}_{pde} = \frac{1}{N_{fluid}} \sum \left[|\mathcal{R}_{mass}|^2 + \frac{|\mathcal{R}_{mom,x}|^2 + |\mathcal{R}_{mom,y}|^2}{\text{Ma}_\infty^2} + \frac{|\mathcal{R}_{energy}|^2}{\text{Ma}_\infty^4} \right] \quad (3 \leq \text{Ma}_\infty) \text{ Type A}$$

$$= \frac{1}{N_{fluid}} \sum_{\text{Type B}} [|\mathcal{R}_{mass}|^2 + (|\mathcal{R}_{mom,x}|^2 + |\mathcal{R}_{mom,y}|^2)Ma_\infty^2 + |\mathcal{R}_{energy}|^2 Ma_\infty^4] \quad (Ma_\infty \leq 2), \quad (20)$$

- **Enthalpy Loss (\mathcal{L}_H):** Mathematically, for a steady inviscid flow with a uniform upstream state, the conservation of total enthalpy ($H = \text{const}$) is inherently satisfied by the energy conservation equation ($\nabla \cdot ((E + p)\mathbf{u}) = 0$). Therefore, the explicit inclusion of the enthalpy loss \mathcal{L}_H appears theoretically redundant. However, in the context of PINN optimization, incorporating this redundant constraint is practically indispensable for three numerical reasons. First, unlike the PDE residuals that require computing noisy and computationally expensive spatial derivatives via Automatic Differentiation (AD), the enthalpy constraint \mathcal{L}_H is a purely algebraic relation evaluated point-wise. It provides a direct, stable gradient signal to anchor the thermodynamic state without the noise of higher-order derivatives. Second, the necessary addition of artificial viscosity ($\nu\Delta\mathbf{U}$) into the PDEs slightly violates strict energy conservation across the shock layer. \mathcal{L}_H continuously corrects this numerical thermodynamic drift, pulling the flow back to the physically correct state. Finally, decoupling this highly non-linear constraint from the stiff spatial PDE losses significantly smooths the optimization landscape, providing a "shortcut" for the optimizer to bypass local minima and accelerate convergence.
- **Nose Region Loss (\mathcal{L}_{nose}):** Evaluated specifically within the azimuthal range $\theta \in [0.9\pi, \pi]$. The expected effect of this localized penalty is to force the optimizer to prioritize the most physically severe region of the flow field—the normal bow shock and the stagnation point. Since the gradients here are exponentially steeper than in the downstream expansion region, uniformly weighted PDE losses often result in a smeared or collapsed shock standoff distance. \mathcal{L}_{nose} counteracts this by acting as a high-resolution magnifying glass, ensuring the strict enforcement of the Rankine-Hugoniot jump and the correct shock detachment distance.
- **Boundary and Stagnation Anchor Losses ($\mathcal{L}_{in}, \mathcal{L}_{wall}, \mathcal{L}_{sym}, \mathcal{L}_{stag}$):** Beyond merely defining the problem space, these boundary constraints provide critical Dirichlet and Neumann anchors that guide the global optimization trajectory. The slip wall condition (\mathcal{L}_{wall}) strictly prevents non-physical mass flux into the solid body, ensuring the correct formation of the high-pressure stagnation pocket. The symmetry loss (\mathcal{L}_{sym}) prevents the neural network from developing asymmetric, non-physical flow biases during the highly stochastic initial phases of the AdamW optimizer. Crucially, the pointwise stagnation constraint (\mathcal{L}_{stag}) at the leading edge $(-0.5, 0)$ anchors the theoretical maximum density and pressure (derived from the Rankine-Hugoniot and isentropic relations). The inclusion of this single point acts as a global thermodynamic calibrator, eliminating the network's uncertainty regarding the amplitude of the compressed flow and significantly accelerating the convergence of the entire downstream field. While the proposed framework successfully achieves fully data-free shock capturing, it is important to acknowledge a specific geometrical limitation inherent in the current stagnation anchor (\mathcal{L}_{stag}) formulation.

Although the macroscopic thermodynamic state (total pressure and total density) at a theoretical stagnation point can be analytically predetermined via the exact Rankine-Hugoniot normal shock relations, identifying the exact spatial coordinates of this stagnation point *a priori* is strictly limited to symmetric configurations aligned with the freestream (e.g., circular cylinders at zero angle of attack). For asymmetric bodies or lifting surfaces, the stagnation point dynamically shifts along the body surface depending on the complex interplay of the emerging flow field, rendering a fixed-point geometric anchor inapplicable prior to solving the equations.

Consequently, the localized application of \mathcal{L}_{stag} in the present study should be viewed as an initial enabling step to isolate and overcome the fundamental optimization pathologies (gradient stiffness and spectral bias) in purely data-free PINNs, rather than a universally applicable geometric boundary condition. Extending this framework to arbitrary asymmetric geometries remains a critical subject for future research. Such extensions may involve developing dynamic anchor localization algorithms—where the loss dynamically tracks the minimum velocity point on the wall—or relying entirely on globally distributed physical invariants, such as entropy conservation along the solid boundaries, without explicitly specifying the stagnation coordinates.

- **Upstream Fixing Mask Loss (\mathcal{L}_{mask}):** Enforces strictly uniform freestream conditions within the upstream region ($x < X_f$), in which X_f is changed in accordance with the theoretical shock detachment distance, which depends on Mach number of the free-stream [20]. In standard PINNs employing symmetric spatial derivatives (via AD), the extreme gradients of the shock wave mathematically "leak" upstream, creating severe non-physical pre-shock oscillations (analogous to the Gibbs phenomenon in central-difference CFD schemes). The expected effect of \mathcal{L}_{mask} is to explicitly break this symmetric information flow. By clamping the upstream region to exact freestream values, it mimics the strict upwinding nature of supersonic flows—ensuring that the flow upstream of the shock remains completely unperturbed by the presence of the downstream obstacle.
- **Total Variation Loss (\mathcal{L}_{tv}):** An azimuthal regularization term $\mathcal{L}_{tv} = \frac{1}{N} \sum |\rho_{\theta+1,r} - \rho_{\theta,r}|$ introduced to explicitly suppress the non-physical carbuncle phenomenon near the stagnation line. While sacrificing a minute degree of strict mass conservation, it acts as essential numerical dissipation. The expected effect of this term is to aggressively damp high-frequency spatial noise along the angular direction, preventing the optimizer from falling into chaotic, corrugated local minima along the shock front, thereby yielding a smooth and physically consistent isentropic expansion around the cylinder.

A fundamental open challenge in the current PINN literature is the determination of the weighting coefficients λ_i for multi-objective loss functions. While various adaptive weighting algorithms—such as Neural Tangent Kernel (NTK)-based scaling or gradient-matching heuristics (e.g., SoftAdapt)—have been successfully applied to smooth elliptic or parabolic PDEs, preliminary investigations revealed that these dynamic weighting schemes catastrophically fail for high-Mach hyperbolic conservation laws.

The presence of a developing shock discontinuity causes sudden and extreme fluctuations in local loss gradients. Adaptive algorithms misinterpret these sharp physical gradients as numerical anomalies, inducing wild oscillations in the loss weights that ultimately destroy the Rankine-Hugoniot jump conditions and lead to divergence. Consequently, unstable adaptive schemes are eschewed in favor of a static, *physics-guided heuristic* approach for the hyperparameters, governed by the following three physical principles:

- i) **Theoretical Internal Balance:** As detailed in the previous section, the most critical balance—the relative weighting among the mass, momentum, and energy PDE residuals—is not determined empirically. Instead, it is rigorously derived via a *regime-dependent, Mach-number-guided dynamic residual scaling*. For high-Mach flows ($\text{Ma}_\infty \geq 3$), the residuals are scaled down ($\mathcal{O}(1/\text{Ma}_\infty^2)$ and $\mathcal{O}(1/\text{Ma}_\infty^4)$) to mathematically pre-condition the most severely stiff components of the Hessian matrix. The Hessian matrix condition number diverges as $\mathcal{O}(\text{Ma}_\infty^4) \rightarrow \infty$, creating an ill-conditioned landscape where L-BFGS leads to severe zig-zagging and premature convergence. This scaling effectively pre-conditions the Hessian matrix, ensuring eigenvalues associated with each loss component converge at a uniform rate. To mathematically elucidate the qualitative scaling of the Hessian matrix $\mathcal{H} \sim \mathcal{O}(\text{Ma}_\infty^4)$ in high-speed regimes, one must consider the Rankine-Hugoniot jump conditions governing the strong shock discontinuity. Across a normal shock wave, the pressure jump Δp and the energy jump ΔE scale quadratically with the freestream Mach number: $\Delta p \sim \mathcal{O}(\text{Ma}_\infty^2)$. Consequently, the spatial gradients of the physical variables within the unresolved shock layer, and thus the unscaled Euler PDE residuals \mathcal{R} , are inherently amplified by this quadratic factor ($\mathcal{R} \sim \mathcal{O}(\text{Ma}_\infty^2)$). In the context of PINNs, the loss function is formulated as the mean squared error of these residuals, $\mathcal{L} \propto \mathcal{R}^2$. The Hessian matrix of the loss function with respect to the network weights θ can be approximated using the Gauss-Newton formulation:

$$\mathcal{H} = \nabla_{\theta}^2 \mathcal{L} \approx 2\mathcal{J}^T \mathcal{J}, \quad (21)$$

where $\mathcal{J} = \nabla_{\theta} \mathcal{R}$ is the Jacobian matrix of the residuals. Since the magnitude of the Jacobian inherently scales with the residual itself ($\mathcal{J} \sim \mathcal{O}(\text{Ma}_\infty^2)$), the resulting Hessian matrix is dominated by the product of these Jacobians. Therefore, the spectral norm of the Hessian exhibits a quartic dependence on the Mach number:

$$\|\mathcal{H}\| \sim \mathcal{O}((\mathcal{J})^2) \sim \mathcal{O}((\text{Ma}_\infty^2)^2) = \mathcal{O}(\text{Ma}_\infty^4). \quad (22)$$

This quartic amplification mathematically explains why the optimization landscape becomes extraordinarily stiff, transforming into pathological plateaus that completely paralyze standard gradient descent algorithms such as AdamW in high-Mach regimes.

Conversely, for low-supersonic flows ($\text{Ma}_\infty \leq 2$), the residuals are scaled up ($\mathcal{O}(\text{Ma}_\infty^2)$ and $\mathcal{O}(\text{Ma}_\infty^4)$) to act as stringent penalty multipliers, effectively forcing the network to overcome its inherent spectral bias.

- ii) **Prioritization of Hard Constraints:** Boundary conditions ($\mathcal{L}_{in}, \mathcal{L}_{wall}, \mathcal{L}_{stag}$) and the upstream mask (\mathcal{L}_{mask}) serve as the fundamental driving forces that define the physical domain. In this protocol, these terms are assigned dominant weights ($\lambda \sim 10^2 - 10^3$) relative to the scaled PDE loss ($\lambda_{pde} = 1$). This strict prioritization forces the optimizer to rapidly carve out the macroscopic boundaries and the correct stagnation pocket before attempting to resolve the complex internal flow field, effectively preventing the network from collapsing into trivial constant-state solutions.
- iii) **Minimization of Artificial Dissipation:** Regularization terms designed to suppress numerical oscillations, such as the TV loss (\mathcal{L}_{tv}), are inherently non-conservative. To ensure they act strictly as weak numerical dissipation without overriding the governing equations, their weights are deliberately constrained to extremely small magnitudes ($\lambda_{tv} \ll 1$).

By combining the rigorous Mach-number scaling for the PDEs with physical intuition for the boundary constraints, this static weighting strategy demonstrates remarkable robustness and reproducibility across the Mach 2 to 15 regimes, bypassing the fragility of automated multi-objective optimization algorithms.

To ensure reproducibility and stable optimization, the static weighting coefficients λ_i are explicitly defined based on physical prioritization. For all Mach numbers except $\text{Ma}_\infty = 15$, the weights are set as follows: $\lambda_{pde} = 1$, $\lambda_H = 0.5$, $\lambda_{in} = 20$, $\lambda_{wall} = 500$, $\lambda_{stag} = 200$, $\lambda_{sym} = 20$, $\lambda_{mask} = 1000$, and $\lambda_{tv} = 0.01$. The weight for the nose region, λ_{nose} , is dynamically adjusted or kept constant depending on the specific case.

Crucially, in the extreme hypersonic regime at $\text{Ma}_\infty = 15$, the strong carbuncle instability necessitates increased numerical dissipation. Therefore, the weight for the Total Variation loss is amplified by a factor of 10, specifically set to $\lambda_{tv} = 0.1$, while all other coefficients remain identical.

Optimization Strategy and Training Protocol

To navigate this ill-conditioned landscape, a curriculum learning strategy and a two-stage hybrid optimization are employed.

Phase 1: Global Exploration via AdamW

Optimizing from a random initialization directly using L-BFGS invariably leads to failure due to its reliance on local curvature. Training is first conducted using the AdamW optimizer for N_A epochs. Concurrently, the artificial viscosity is annealed from $\nu = 0.01$ down to $\nu = 0.0005$ over the first N_{AN} epochs. This phase establishes the macroscopic physical structure of the flow and steers the parameters into the global basin of attraction.

Phase 2: Local Exploitation via L-BFGS

Once AdamW locates the correct basin, optimization is handed to L-BFGS. Operating within a smooth, convex-like region, L-BFGS performs highly accurate Newton-like steps to aggressively sharpen the shock discontinuity. However, because all network computations are strictly executed in single-precision floating-point format ('float32'),

the numerical resolution of the loss function is inherently bounded by a machine epsilon of approximately 10^{-6} . Consequently, the L-BFGS solver is configured to terminate automatically either when the loss value drops below this single-precision threshold (as smaller variations cannot be meaningfully resolved) or when the relative decrease in the loss function stagnates and ceases to progress across successive iterations.

Generation of CFD Reference Solutions

To rigorously evaluate the predictive accuracy of the proposed data-free PINN framework, high-fidelity reference solutions were generated using a conventional Computational Fluid Dynamics (CFD) approach. The steady-state 2D compressible inviscid Euler equations were solved using a cell-centered Finite Volume Method (FVM).

To ensure robust shock-capturing capabilities across the wide range of Mach numbers ($2 \leq \text{Ma}_\infty \leq 15$), the convective fluxes at the cell interfaces were evaluated using the HLLC (Harten-Lax-van Leer-Contact) approximate Riemann solver [21]. The choice of the HLLC scheme is particularly critical for high-Mach blunt body flows, as it inherently resists the non-physical carbuncle instability near the stagnation point. To achieve second-order spatial accuracy while strictly preventing spurious numerical oscillations near the strong bow shock discontinuities, a MUSCL (Monotone Upstream-centered Schemes for Conservation Laws) data reconstruction strategy [22] was employed in conjunction with a standard slope limiter. The time integration to reach the steady state was accelerated using an implicit LU-SGS (Lower-Upper Symmetric Gauss-Seidel) method.

The computational domain was strictly matched to the PINN setup and discretized by a highly refined, body-fitted structured mesh consisting of 200(radial direction) \times 50(azimuthal direction) grid points. Grid clustering was explicitly applied near the cylinder surface and the anticipated bow shock region to guarantee an extremely sharp, grid-converged shock resolution, serving as an exact physical baseline against which the PINN’s predictive fidelity could be quantitatively assessed.

Computational Cost and Efficiency Considerations

To provide a transparent assessment of the computational requirements, the wall-clock times of the proposed PINN framework and the conventional CFD approach are compared. All neural network training processes were executed on a single NVIDIA GeForce GTX 1070 GPU. The global exploration phase using the AdamW optimizer (20,000 epochs) requires approximately 4 hours of computational time, while the subsequent L-BFGS phase maintains a comparable computational cost per iteration. In contrast, the conventional FVM-based CFD simulation, even for the most demanding hypersonic regime at $\text{Ma}_\infty = 15$, achieves steady-state convergence in approximately 30 minutes on a standard CPU.

While the current PINN framework exhibits a higher computational overhead for single forward simulations compared to highly optimized, mature CFD solvers, it

is crucial to emphasize that the primary objective of this study is not to accelerate steady-state forward solvers. Rather, the focus is on mathematically overcoming the fundamental optimization barriers—namely, gradient stiffness and spectral bias—that have historically prevented purely data-free PINNs from resolving extreme shock discontinuities. By successfully establishing a stable, regime-independent optimization methodology without relying on any external reference data, this work provides a critical foundational step. The theoretical insights and the hybrid convolutional architecture developed herein pave the way for future advanced applications, such as parameterized surrogate modeling and inverse problem resolution, where the initial offline training cost is overwhelmingly offset by the capability of rapid, differentiable online inferences.

Results

Baseline Comparison: The Impact of Spatial Inductive Bias

The inability of the standard MLP to capture the shock discontinuity, as observed in the baseline results, is consistent with the theory of *Spectral Bias* in neural networks [4]. Theoretical works using the Neural Tangent Kernel (NTK) analysis have established that fully connected networks exhibit a strong bias towards learning low-frequency functions, with the convergence rate of high-frequency components decaying polynomially [19, 23]. In the context of hypersonic flows, a shock wave represents a step-like function containing infinite high-frequency modes. Wang et al. [24] specifically pointed out that this spectral bias is a primary cause of training failure in PINNs, where stiff gradient components (such as shocks) are often ignored during optimization. Empirical results confirm this theoretical prediction: the MLP effectively acts as a low-pass filter, smoothing out the sharp shock front into a diffuse gradient to satisfy the smoothness prior inherent in its architecture. Crucially, the proposed hybrid CNN architecture overcomes this limitation not by mere hyperparameter tuning, but by introducing a spatial inductive bias. To rigorously evaluate the necessity and effectiveness of the proposed hybrid convolutional architecture, a comparative baseline is established using a standard Multi-Layer Perceptron (MLP).

To rigorously evaluate the necessity and effectiveness of the proposed hybrid convolutional architecture, a comparative baseline is established using a standard Multi-Layer Perceptron (MLP). To ensure a fair comparison, the baseline MLP is configured to possess a comparable number of trainable parameters (e.g., 6 hidden layers with 64 neurons each) and employs the exact same activation functions, Mach-number scaling, loss weights, and AdamW-to-L-BFGS optimization protocol at $Ma = 5$ ($N_A = 1.5 \times 10^4$, $N_{\text{an}} = 10^4$).

The progression of density contours predicted by this baseline MLP across training epochs is explicitly illustrated in Fig. 3. In the early optimization stages (the AdamW exploration phase), the network exhibits a vague and unphysical density field. Crucially, even as the computation advances through tens of thousands of epochs, the MLP completely fails to form any structure resembling a shock wave. As shown in the figure, rather than sharpening into a distinct discontinuity, the density distribution progressively morphs into an increasingly irregular and distorted shape over successive

generations. It fails to construct any discernible physical boundary, instead deteriorating into a non-physical, highly distorted flow pattern ahead of the cylinder. This specific visual evidence strongly corroborates the theoretical premise: the failure of the MLP is not merely a matter of excessive numerical diffusion, but rather stems from the challenging optimization landscape of data-free PINNs coupled with the well-documented *spectral bias* of fully connected networks [4]. Without the geometric "awareness" provided by a directional inductive bias, the MLP struggles to balance the competing boundary conditions and conservation laws. Constrained by its bias toward low-frequency representations, it is completely unable to localize the sharp high-frequency gradients. Consequently, the optimizer is forced into a highly pathological local minimum, producing a globally distorted and non-physical field simply to artificially minimize the residual losses.

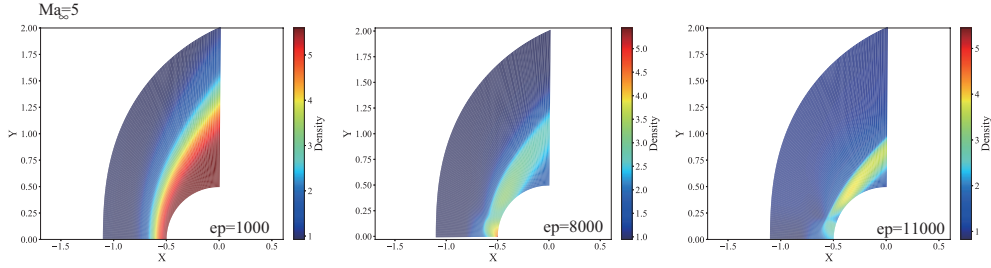


Fig. 3 Snapshots of density contours across training epochs ($ep=10^3$, 8×10^3 and 1.1×10^4) obtained using baseline MLP.

Detailed Validation and Physical Discrepancies in Supersonic to Hypersonic Regimes ($3 \leq Ma_\infty \leq 15$)

In this section, the physical fidelity of the proposed data-free PINN framework is validated across a broad range of supersonic and hypersonic regimes ($3 \leq Ma_\infty \leq 15$). Concurrently, a detailed comparative analysis against CFD reference solutions is provided to elucidate the localized physical discrepancies inherent to PINNs that manifest as the Mach number increases.

Shock Layer Structures and Stand-off Distance (Fig. 4)

Figure 4 presents the two-dimensional macroscopic flow fields—specifically, the contours of density, Mach number, temperature, and pressure—around the cylinder for various freestream Mach numbers ($Ma_\infty = 3, 5, 9, 11, 13, 15$). To facilitate a direct visual comparison, each panel is symmetrically divided: the upper half ($Y > 0$) displays the predictions generated by the data-free PINN type A, while the lower half ($Y < 0$) shows the corresponding CFD reference solutions.

As a general trend, the PINN type A successfully captures the macroscopic structure of the detached bow shock without relying on external reference data. Notably, as the Mach number increases from $Ma_\infty = 3$ to $Ma_\infty = 15$, the shock stand-off distance gradually decreases, and the shock front approaches the cylinder surface—accurately reflecting the fundamental nature of compressible aerodynamics. This confirms that

the proposed hybrid convolutional architecture correctly embeds spatial and geometric relationships. Furthermore, contour distortions near the stagnation point (i.e., the carbuncle phenomenon) are effectively suppressed, demonstrating the contribution of the TV loss to macroscopic stability.

Profiles and Velocity Discrepancies along the Stagnation Streamline (Fig. 5)

To conduct a detailed quantitative evaluation of the flow field, Figure 5 presents the profiles of density, velocity, temperature, and pressure along the stagnation streamline ($Y = 0$) for both the PINN type A and CFD. For reference, the exact analytical solutions for density and pressure at the stagnation point ($X = -0.5, Y = 0$) are also plotted as distinct points. A close inspection of these profiles reveals that as the Mach number increases, the PINN type A solutions begin to locally diverge from the exact CFD solutions.

1. Behavior in Moderate Supersonic and Hypersonic Regimes ($Ma_\infty = 3, 5$)

For the cases of $Ma_\infty = 3$ and $Ma_\infty = 5$, the PINN type A predictions (solid lines) exhibit excellent agreement with both the CFD reference data (dashed lines) and the analytical exact solutions at the stagnation point. The sharp jump at the shock front, followed by the pressure rise and velocity deceleration leading up to the cylinder surface, faithfully traces the theoretical behavior. In this regime, the Mach-number-guided scaling and artificial viscosity function in optimal balance.

2. Non-linearization and Discrepancy of Velocity Profiles in High-Mach Regimes ($Ma_\infty \geq 9$)

Conversely, as the flow enters more extreme hypersonic regimes ($Ma_\infty = 9, 11, 13$) and culminates at $Ma_\infty = 15$, significant discrepancies emerge in the distribution of physical quantities within the shock layer. The most emblematic of these is the behavior of the velocity profile. As indicated by the CFD solutions, the subsonic flow immediately following the shock front should physically decelerate toward the stagnation point in a nearly linear fashion (i.e., with a constant spatial gradient). However, the velocity profile predicted by the PINN type A gradually loses this linearity as the Mach number increases through 9, 11, and 13, eventually tracing a non-linear, convex-upward deceleration curve downstream. Consequently, the PINN type A locally overestimates the velocity within the shock layer compared to the CFD, resulting in a clear deviation between the two.

Physical and Mathematical Origins of the Discrepancies

This non-linearization of the velocity profile and the resulting mismatch with CFD are considered artifacts of the PINN type A arising from the optimization dilemma unique to high-Mach-number flows. This phenomenon is attributed to an interplay of two primary factors:

First, the **excessive smoothing effect of artificial viscosity and TV loss**. Quantitatively, for the range of $3 \leq Ma_\infty \leq 13$, the thickness of the shock layer remains relatively confined and sharp, falling within a range of 0.05 to 0.075. However, this is not the case for $Ma_\infty = 15$. To suppress the severe carbuncle instability at this extreme condition, the weight of the TV loss is intentionally amplified by a factor of 10 compared to the other cases. It is postulated that this aggressive spatial smoothing penalty significantly increases the numerical viscosity, causing the shock wave

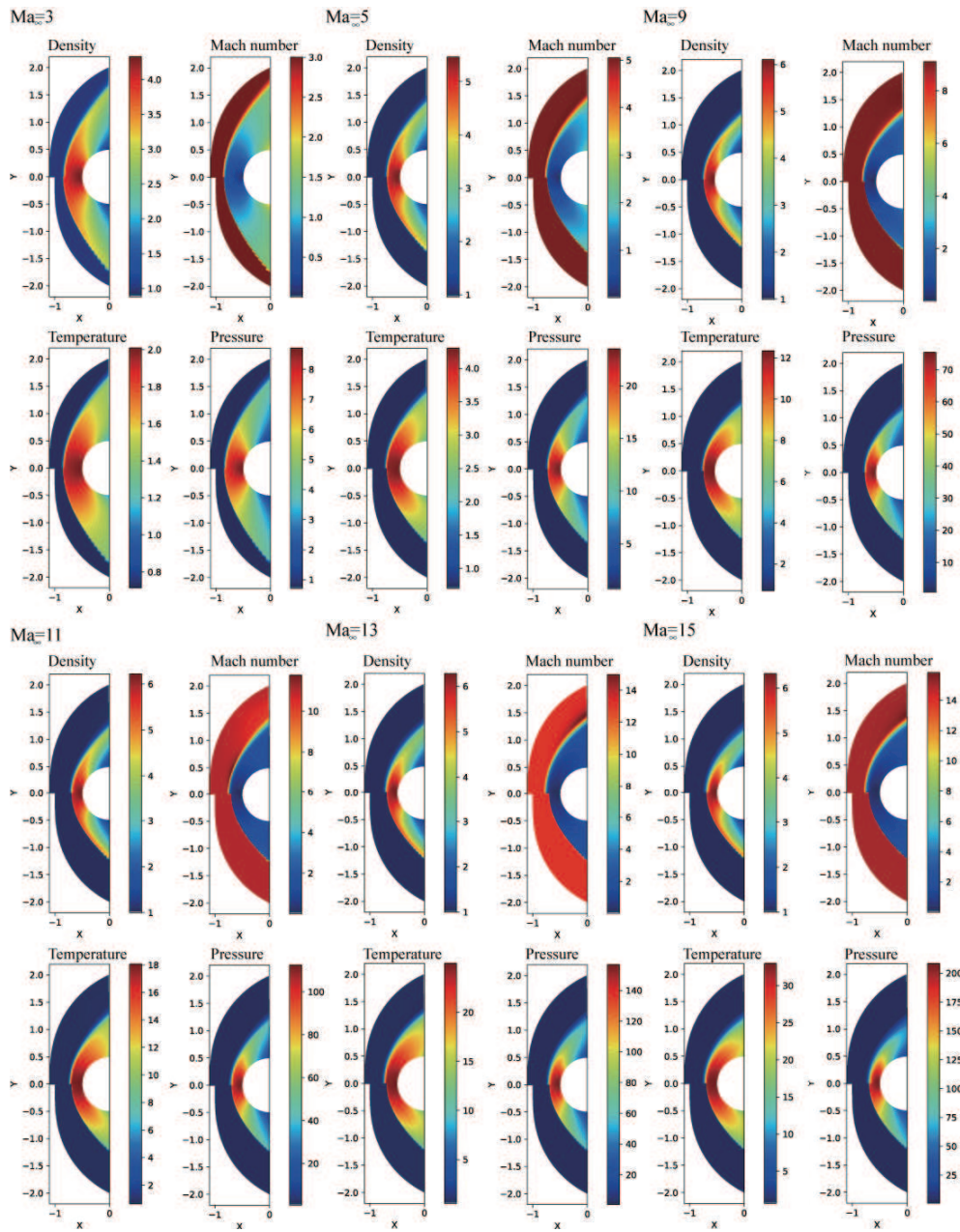


Fig. 4 Contours of density, Mach number, temperature, and pressure for various Mach numbers ($Ma = 3, 5, 9, 11, 13$ and 15). Top halves ($0 \leq Y$) show PINN type A predictions; bottom halves ($Y \leq 0$) show CFD reference solutions.

thickness at $Ma_\infty = 15$ to broaden to approximately 0.1. This excessive numerical dissipation not only thickens the shock front but also overly smooths the minute velocity gradient (which should mathematically maintain a linear deceleration) inside the shock layer, thereby distorting it into a non-linear curve.

Second, the **relative weakening of the momentum loss due to scaling**. To prevent gradient explosion in the hypersonic regime, the energy and momentum equations were drastically scaled down by factors of the Mach number (Ma_∞^4 and Ma_∞^2 , respectively). While this strategy averts complete training failure, the severity of this scaling intensifies as the Mach number grows ($Ma_\infty = 9, 11, 13 \dots$), relatively relaxing the strictness of momentum conservation near the stagnation point. As a result, the neural network tends to "compromise" by prioritizing the minimization of mass conservation (density) and boundary condition losses, inadvertently shifting the residual error into the velocity profile. Indeed, corresponding to the region where the velocity overshoots the CFD profile, the predicted temperature is concurrently underestimated. This indicates that the conversion process from kinetic energy to internal energy is locally delayed (or smeared) within the shock layer.

In conclusion, while the proposed data-free PINN type A is highly effective at capturing macroscopic shock structures, it reveals a fundamental limitation in severe hypersonic regimes ($Ma_\infty \geq 9$). The "smoothing" (via TV loss and artificial viscosity) and "residual scaling" necessitated for optimization stability come at the cost of inducing non-linear discrepancies in variables such as the stagnation streamline velocity profile. This finding exposes a critical boundary in the ability of purely data-free PINNs to flawlessly satisfy strict physical conservation laws within hypersonic shock layers.

Convergence Analysis and Optimization Dynamics Across Mach Numbers

To comprehensively evaluate the training stability and optimization dynamics of the proposed framework, Figure 6 presents the convergence history of the total loss function across successive training epochs for various free-stream Mach numbers ($3 \leq Ma_\infty \leq 15$). The optimization strategy employs a robust two-stage protocol: an initial global exploration phase using the AdamW optimizer, followed by a fine-tuning phase employing the second-order L-BFGS algorithm.

Initial Exploration Phase (AdamW Optimizer)

During the AdamW optimization phase, the total loss exhibits a rapid and stable initial decay across all Mach regimes. This stable convergence in the early generations is a direct consequence of the proposed Mach-number-guided residual scaling. Without this critical scaling, the extreme gradient stiffness inherent to hypersonic flows ($Ma_\infty \geq 9$) would typically induce immediate gradient explosion or divergence. Instead, the loss histories demonstrate that the network successfully navigates the highly non-convex loss landscape, gradually localizing the detached shock wave. As expected, higher Mach numbers exhibit a slightly higher resistance to loss minimization during this phase, reflecting the severe physical discontinuities and the intense stiffness of the energy conservation laws.

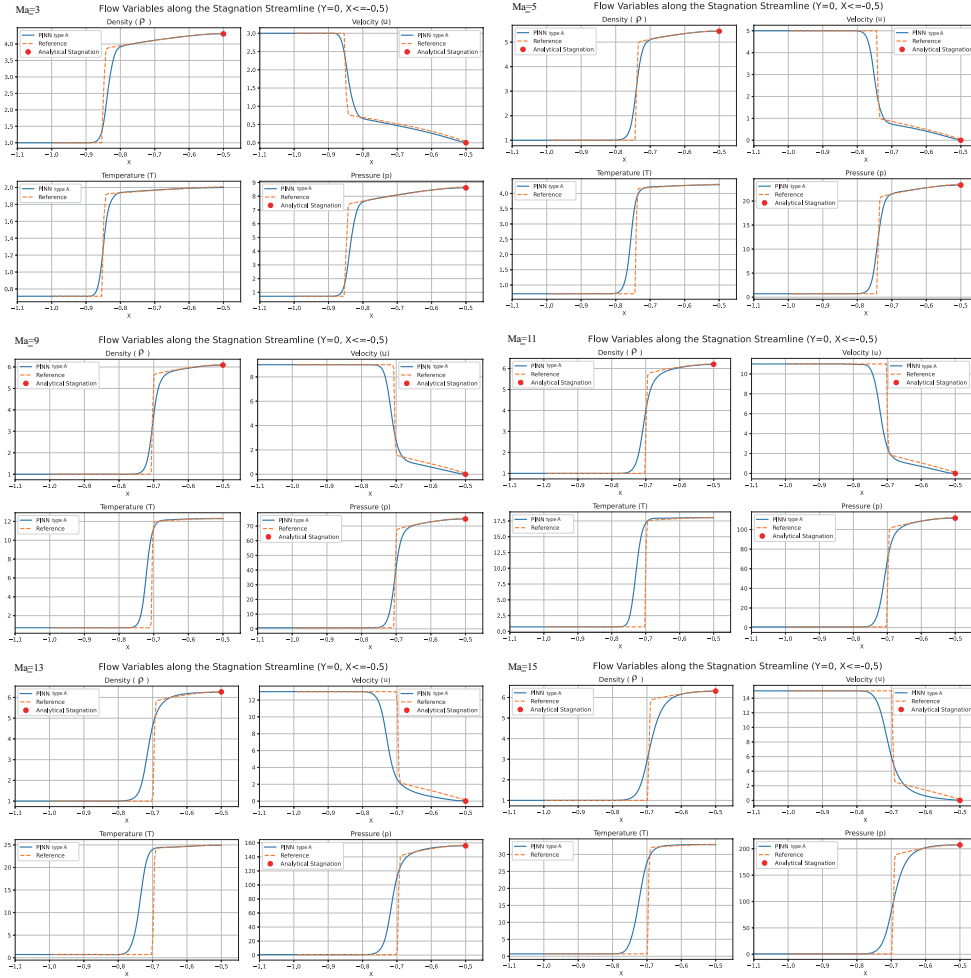


Fig. 5 Profiles of physical quantities (ρ , u , T and p) along the stagnation streamline ($Y = 0$) comparing PINN type A predictions with CFD references.

Fine-Tuning Phase (L-BFGS Optimizer) and Early Termination

Upon transitioning from the AdamW optimizer to the L-BFGS algorithm, an interesting optimization behavior is observed across the Mach numbers: the L-BFGS optimization phase is remarkably short, appearing almost non-existent in the convergence history. This absence is due to the fact that the L-BFGS computation terminates almost immediately (near the 0-th iteration of this phase) because the loss value barely changes from the point of transition.

Mathematically, this early termination occurs because the AdamW optimizer has already navigated the network into a highly stiff and extremely narrow local plateau, which is characteristic of the hyperbolic Euler equations with shock discontinuities. Consequently, the relative change in the loss function falls below the strict tolerance threshold of the L-BFGS algorithm, causing its line search mechanism to fail to find

a better step direction and forcing an early exit. This implies that the final converged physical fields and residual levels are almost entirely determined by the initial AdamW exploration phase.

When analyzing this final plateau of the converged loss values, a clear Mach-number dependency emerges. The cases with moderate supersonic speeds ($Ma_\infty = 3$ and 5) converge to the lowest final residuals. Conversely, as the Mach number enters the extreme hypersonic regime ($Ma_\infty \geq 9$), the final converged loss settles at progressively higher values. It is crucial to emphasize that the elevated final loss at $Ma_\infty = 15$ is a mathematical reflection of the intensely stiff shock layer combined with the heavily amplified Total Variation (TV) loss penalty (multiplied by a factor of 10). The network is forced into a structural trade-off: it maintains macroscopic stability and successfully suppresses the carbuncle phenomenon at the justifiable expense of a slightly higher baseline residual, leading to the immediate termination of the L-BFGS solver.

Mach-Guided Scaling and Spectral Bias in the Low-Supersonic Regime ($Ma_\infty = 2$)

To further investigate the regime-dependent nature of optimization dynamics in data-free PINNs, the low-supersonic flow over the cylinder at $Ma_\infty = 2$ is examined using PINNs type A and B. Figures 7 and 8 present a comparative analysis between two distinct residual scaling strategies, PINNs type A and B against the CFD reference solution.

As clearly illustrated in the figures, PINN type A completely fails to accurately resolve the shock layer. The resulting flow-field is highly smeared and significantly deviates from the reference CFD solution. This failure can be mathematically attributed to the inherent *spectral bias* of neural networks. At $Ma_\infty = 2$, the shock wave is relatively weak, and the unscaled PDE residuals are not excessively large. By dividing these already moderate residuals by Ma_∞^2 and Ma_∞^4 , Type A critically weakens the physical constraints. Consequently, the optimizer takes the "path of least resistance," favoring a non-physical, overly smooth solution to easily minimize boundary conditions and artificial viscosity losses, while effectively ignoring the inviscid conservation laws.

Conversely, PINN type B demonstrates an excellent approximation of the reference CFD solution. By multiplying the PDE residuals by Ma_∞^2 and Ma_∞^4 (which act as factors of 4 and 16, respectively), Type B imposes a stringent mathematical penalty on the optimizer. This intense physical constraint forces the neural network to strictly adhere to the inviscid Euler equations and the Rankine-Hugoniot jump conditions, preventing it from smoothing out the weak discontinuity.

These comparative results underscore a fundamental and novel finding of this study: optimal loss balancing in compressible PINNs is highly regime-dependent. While scaling down (division) is an absolute prerequisite to prevent gradient explosion in hypersonic regimes ($Ma_\infty \geq 5$), introducing penalty multipliers (multiplication) is conversely imperative to overcome spectral bias and enforce physical fidelity in low-supersonic flows ($Ma_\infty = 2$).

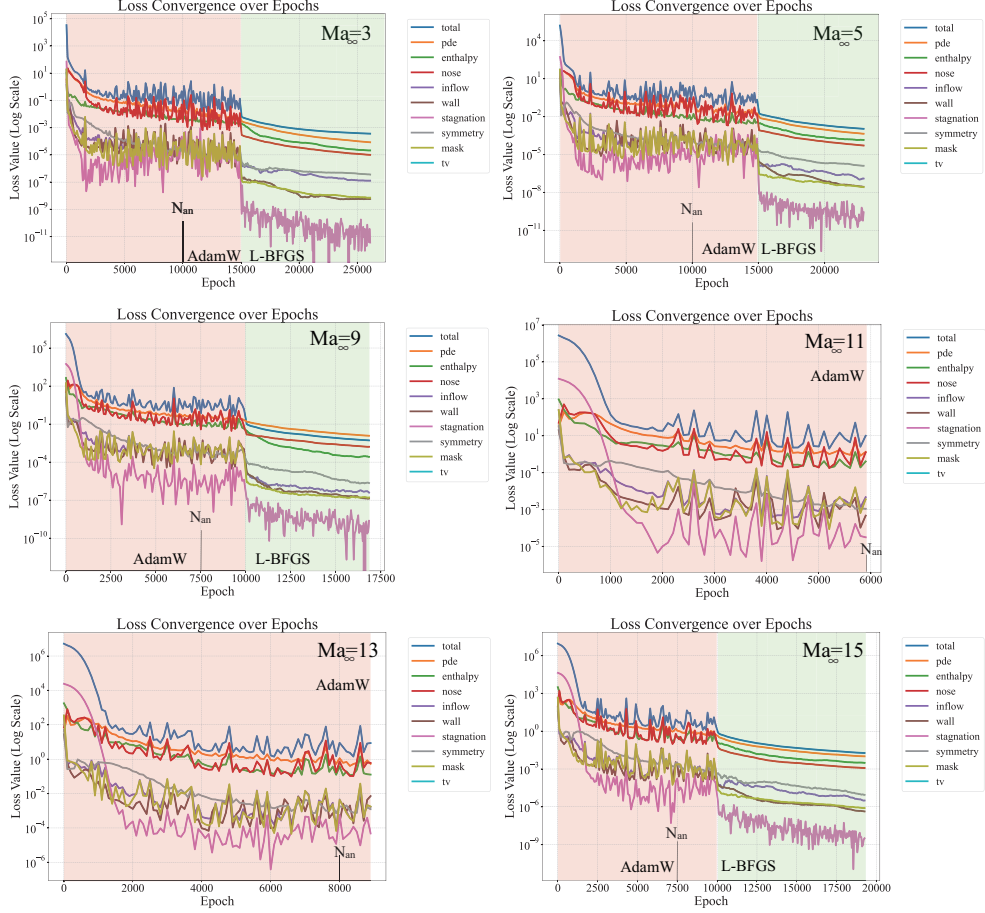


Fig. 6 Convergence history of the total composite loss function across successive training epochs for varying freestream Mach numbers ($3 \leq Ma_\infty \leq 15$). The optimization trajectory is visually partitioned into two distinct stages: the red shaded region illustrates the global exploration phase driven by the AdamW optimizer, while the green shaded region corresponds to the local fine-tuning phase executed by the L-BFGS algorithm. The explicit marker N_{an} denotes the exact epoch at which the artificial viscosity annealing protocol is completed, locking the numerical dissipation to its minimum threshold. The virtually instantaneous termination of the L-BFGS phase in high-Mach regimes visually corroborates that the optimizer is forced into an extremely narrow, stiff local plateau by the conclusion of the AdamW phase.

Conclusion

This paper proposed and validated a fully data-free PINN framework capable of resolving compressible inviscid flows around a circular cylinder across a wide range of supersonic and hypersonic regimes ($2 \leq Ma_\infty \leq 15$), without relying on any external reference data. To overcome the "spatial blindness" inherent in standard MLPs, a hybrid convolutional architecture combining radial 1D convolutions with anisotropic azimuthal 2D convolutions was introduced. This structural design successfully embeds

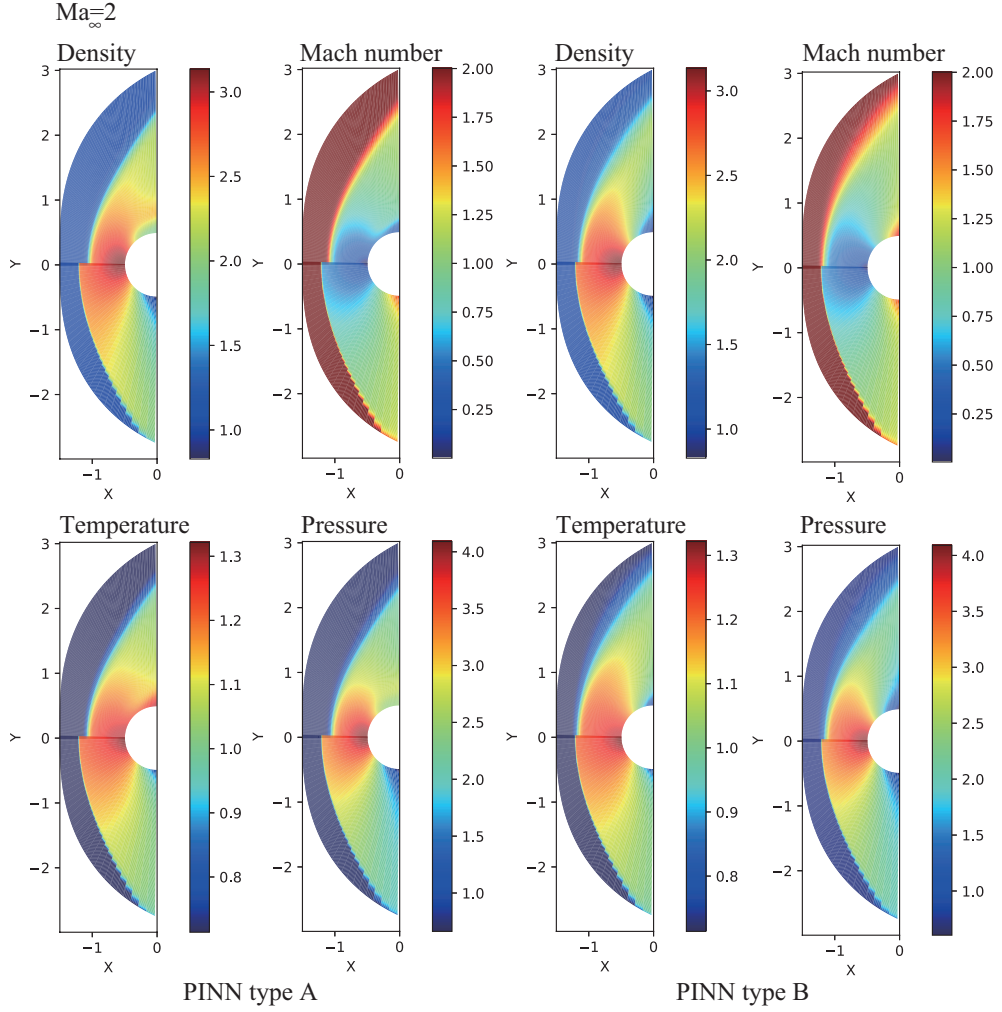


Fig. 7 Comparison of density at $Ma_\infty = 2$ obtained using PINNs type A and B ($0 \leq Y$) with their reference CFD solution ($Y \leq 0$).

directional geometric inductive biases into the network, enabling the accurate capture of the macroscopic structures of detached bow shocks.

The most significant and novel finding of this study is that the optimal loss balancing strategy in compressible PINNs is fundamentally regime-dependent. In regimes ($3 \leq Ma$), dividing the partial differential equation (PDE) residuals by factors of the Ma (scaling down) is an absolute prerequisite to prevent extreme gradient explosion driven by momentum and kinetic energy dominance. Conversely, in the low-supersonic regime ($Ma = 2$), it was revealed that the network suffers from *spectral bias*, tending to ignore weak physical discontinuities in favor of excessively smooth solutions. To overcome this, the PDE residuals must be multiplied by powers of the Mach number (Ma^2 , Ma^4) to amplify the penalty (scaling up), thereby forcing the optimizer to

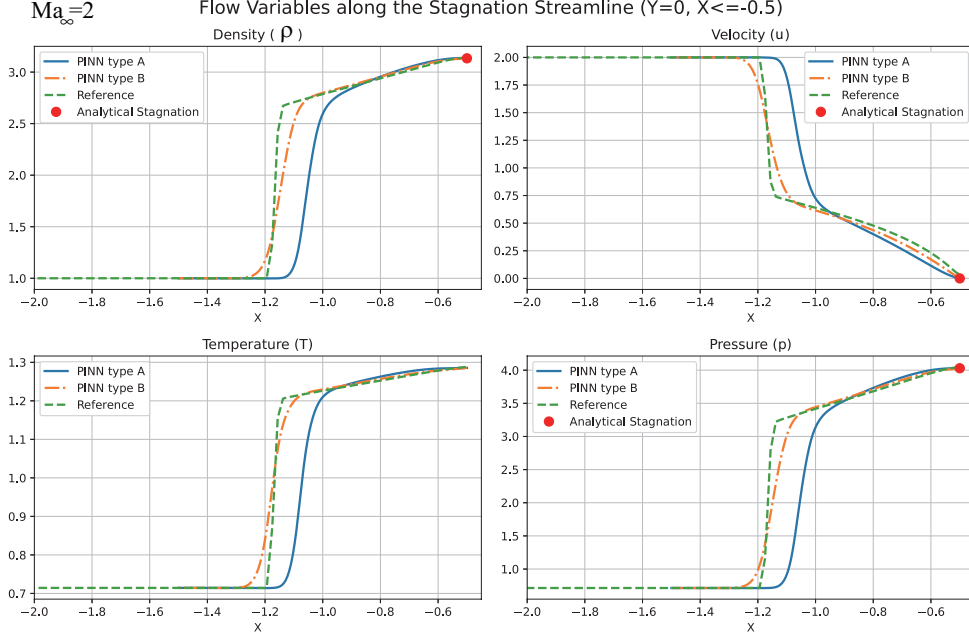


Fig. 8 Comparison of profiles of density, velocity, temperature and pressure along the stagnation streamline obtained using PINNs type A and B with their reference CFD solution, when $Ma_\infty = 2$.

strictly adhere to physical fidelity.

Furthermore, the integration of artificial viscosity, Total Variation (TV) loss, and a novel "Upstream Fixing" boundary loss proved highly effective in achieving global convergence during the two-stage optimization process (transitioning from AdamW to L-BFGS) and in suppressing the non-physical carbuncle phenomenon near the stagnation point. However, the inherent limitations and trade-offs of purely data-free PINNs were also quantitatively demonstrated. The mathematical smoothing penalties required to stabilize the optimization – particularly at the extreme $Ma_\infty = 15$ condition, where the TV loss weight was amplified by a factor of 10 – inevitably smear the shock front and induce non-linear discrepancies in variables such as the velocity profile along the stagnation streamline.

In summary, while the proposed method may not yet achieve the exact, infinitely sharp shock resolution of traditional Computational Fluid Dynamics (CFD) schemes, it demonstrates unprecedented optimization stability and physical validity for data-free PINNs in extreme aerodynamic environments. The integration of "Mach-number-guided dynamic scaling" and the "hybrid convolutional architecture" presented in this study establishes a crucial mathematical and physical foundation for the future practical application of PINNs to more complex compressible flow problems.

Data availability

The data generated in this study are available from the corresponding author upon request.

References

- [1] Raissi, M., Perdikaris, P. & Karniadakis, G. E. Physics-informed neural networks: A deep learning framework for solving forward and inverse problems involving nonlinear partial differential equations. *Journal of Computational physics* **378**, 686–707 (2019).
- [2] Cybenko, G. Approximation by superpositions of a sigmoidal function. *Mathematics of control, signals and systems* **2**, 303–314 (1989).
- [3] Jin, X., Cai, S., Li, H. & Karniadakis, G. E. Nsfnets (navier-stokes flow nets): Physics-informed neural networks for the incompressible navier-stokes equations. *Journal of Computational Physics* **426**, 109951 (2021).
- [4] Rahaman, N. *et al.* *On the spectral bias of neural networks*, 5301–5310 (PMLR, 2019).
- [5] Chaumet, A. & Giesselmann, J. Improving weak pinns for hyperbolic conservation laws: Dual norm computation, boundary conditions and systems. *arXiv preprint arXiv:2211.12393* (2022).
- [6] Mizuno, Y., Misaka, T. & Furukawa, Y. Physics-informed neural network modeling of shock waves by appropriately incorporating equation of state. *Scientific Reports* (2026).
- [7] Ferrer-Sánchez, A., Martín-Guerrero, J. D., de Austri-Bazan, R. R., Torres-Forné, A. & Font, J. A. Gradient-annihilated pinns for solving riemann problems: Application to relativistic hydrodynamics. *Computer Methods in Applied Mechanics and Engineering* **424**, 116906 (2024).
- [8] Mao, Z., Jagtap, A. D. & Karniadakis, G. E. Physics-informed neural networks for high-speed flows. *Computer Methods in Applied Mechanics and Engineering* **360**, 112789 (2020).
- [9] Liu, L. *et al.* Discontinuity computing using physics-informed neural networks. *Journal of Scientific Computing* **98**, 22 (2024).
- [10] Wassing, S., Langer, S. & Bekemeyer, P. Physics-informed neural networks for transonic flows around an airfoil. *arXiv preprint arXiv:2408.17364* (2024).
- [11] Michoski, C., Milosavljević, M., Oliver, T. & Hatch, D. R. Solving differential equations using deep neural networks. *Neurocomputing* **399**, 193–212 (2020).

- [12] Cai, S., Wang, Z., Wang, S., Perdikaris, P. & Karniadakis, G. E. Physics-informed neural networks for heat transfer problems. *Journal of Heat Transfer* **143**, 060801 (2021).
- [13] Jagtap, A. D., Mao, Z., Adams, N. & Karniadakis, G. E. Physics-informed neural networks for inverse problems in supersonic flows. *Journal of Computational Physics* **466**, 111402 (2022).
- [14] Gao, H., Sun, L. & Wang, J.-X. Phygeonet: Physics-informed geometry-adaptive convolutional neural networks for solving parameterized steady-state pdes on irregular domain. *Journal of Computational Physics* **428**, 110079 (2021).
- [15] Quirk, J. J. A contribution to the great riemann solver debate. *International Journal for numerical methods in fluids* **18**, 555–574 (1994).
- [16] Wang, S., Teng, Y. & Perdikaris, P. Understanding and mitigating gradient flow pathologies in physics-informed neural networks. *SIAM Journal on Scientific Computing* **43**, A3055–A3081 (2021).
- [17] Yano, R., Suzuki, K. & Kuroda, H. Formulation and numerical analysis of diatomic molecular dissociation using boltzmann kinetic equation. *Physics of Fluids* **19** (2007).
- [18] Yano, R., Suzuki, K. & Kuroda, H. Formulation and numerical analysis of vibrationally coupled recombination of monatomic molecules using boltzmann kinetic equation. *Physics of Fluids* **21** (2009).
- [19] Jacot, A., Gabriel, F. & Hongler, C. Neural tangent kernel: Convergence and generalization in neural networks. *Advances in neural information processing systems* **31** (2018).
- [20] Billig, F. S. Shock-wave shapes around spherical-and cylindrical-nosed bodies. *Journal of Spacecraft and Rockets* **4**, 822–823 (1967).
- [21] Toro, E. F., Spruce, M. & Speares, W. Restoration of the contact surface in the hll-riemann solver. *Shock waves* **4**, 25–34 (1994).
- [22] Van Leer, B. Towards the ultimate conservative difference scheme. v. a second-order sequel to godunov’s method. *Journal of computational Physics* **32**, 101–136 (1979).
- [23] Tancik, M. *et al.* Fourier features let networks learn high frequency functions in low dimensional domains. *Advances in neural information processing systems* **33**, 7537–7547 (2020).
- [24] Wang, S., Yu, X. & Perdikaris, P. When and why pinns fail to train: A neural tangent kernel perspective. *Journal of Computational Physics* **449**, 110768

(2022).